Article

Singular dielectric nanolaser with atomic-scale field localization

https://doi.org/10.1038/s41586-024-07674-9

Received: 9 February 2024

Accepted: 5 June 2024

Published online: 17 July 2024

Check for updates

Yun-Hao Ouyang[1,4], Hong-Yi Luan[1,4], Zi-Wei Zhao[1,4], Wen-Zhi Mao[1] & Ren-Min Ma[1,2,3] ✉

Compressing the optical field to the atomic scale opens up possibilities for directly observing individual molecules, offering innovative imaging and research tools for both physical and life sciences. However, the diffraction limit imposes a fundamental constraint on how much the optical field can be compressed, based on the achievable photon momentum[1,2]. In contrast to dielectric structures, plasmonics offer superior field confinement by coupling the light field with the oscillations of free electrons in metals[3–6]. Nevertheless, plasmonics suffer from inherent ohmic loss, leading to heat generation, increased power consumption and limitations on the coherence time of plasmonic devices[7,8]. Here we propose and demonstrate singular dielectric nanolasers showing a mode volume that breaks the optical diffraction limit. Derived from Maxwell's equations, we discover that the electric-field singularity sustained in a dielectric bowtie nanoantenna originates from divergence of momentum. The singular dielectric nanolaser is constructed by integrating a dielectric bowtie nanoantenna into the centre of a twisted lattice nanocavity. The synergistic integration surpasses the diffraction limit, enabling the singular dielectric nanolaser to achieve an ultrasmall mode volume of about $0.0005\lambda^3$ (λ, free-space wavelength), along with an exceptionally small feature size at the 1-nanometre scale. To fabricate the required dielectric bowtie nanoantenna with a single-nanometre gap, we develop a two-step process involving etching and atomic deposition. Our research showcases the ability to achieve atomic-scale field localization in laser devices, paving the way for ultra-precise measurements, super-resolution imaging, ultra-efficient computing and communication, and the exploration of light–matter interactions within the realm of extreme optical field localization.

Since the invention of lasers in 1960[9], the localization of the optical field in dimensions such as frequency, time, momentum or space to achieve higher-performance lasers has been a core driving force behind the development of laser physics and devices. The emergence of those high-performance lasers has profoundly contributed to the advancement of modern science and technology. For example, extreme localization of the optical field in the frequency dimension has resulted in frequency-stable lasers necessary for constructing precise interference devices, making gravitational-wave detection possible[10]. In the time dimension, extreme localization of the optical field has led to the development of ultrafast attosecond lasers[11], enabling the observation of ultrafast motion of particles in the microscopic world. In the momentum dimension, extremely localized optical fields yield highly collimated lasers applicable to long-distance interstellar space communication[12]. In the spatial dimension, field localization leads to the development of microscale lasers, with research dating back to the 1990s[13,14]. The ongoing endeavour to achieve ever-smaller lasers persists today, driven by the exploration of the limits of spatial field localization and its practical applications across various fields[15–36].

The uncertainty relationship between momentum and position determines the extent to which we can spatially localize the optical field. For the purpose of constructing extremely small mode volumes, the fundamental obstacle lies in the fact that optical-band semiconductor materials typically have dielectric constants below 10. According to the uncertainty relationship, with such small dielectric constants, we can only localize the optical field to the scale of hundreds of nanometres[1,2]. By coupling the optical field with the oscillations of free electrons in metals, one can achieve plasmonic field confinement[3–6,37–41]. In 2009, plasmonic nanolasers that break the optical diffraction limit were experimentally demonstrated[42–44]. Over the past decade, plasmonic nanolasers have been shown to exhibit extremely small volumes, ultrafast modulation speeds and extremely low energy consumption[15,16,18,19].

However, plasmonic field confinement inevitably comes with inherent ohmic losses[7,8]. The ideal scenario of achieving subdiffraction-limited optical field confinement in dielectrics has long been considered impossible, but this perception has recently changed. Full-wave simulations have indicated that the integration of a dielectric bowtie nanoantenna into a photonic crystal structure can lead to a

[1]State Key Laboratory for Mesoscopic Physics and Frontiers Science Center for Nano-optoelectronics, School of Physics, Peking University, Beijing, China. [2]Peking University Yangtze Delta Institute of Optoelectronics, Nantong, China. [3]National Biomedical Imaging Center, Peking University, Beijing, China. [4]These authors contributed equally: Yun-Hao Ouyang, Hong-Yi Luan, Zi-Wei Zhao. ✉e-mail: renminma@pku.edu.cn

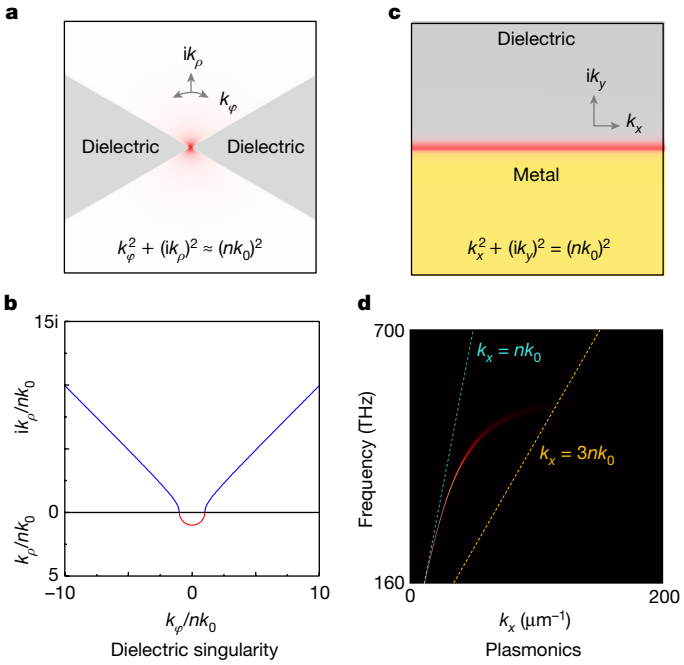

Fig. 1 | Electrical-field infinite singularity in singular dielectric nanolasers. The nanolaser is constructed by integrating a dielectric bowtie nanoantenna, which sustains an electric-field singularity which originates from the divergence of momentum, into the centre of a twisted lattice nanocavity. On the basis of Maxwell's equations, we find that dielectric nanoantennas have an electromagnetic eigenmode characterized by an infinite singularity of the electric field at their apices. This phenomenon arises from the interplay of momenta involved, wherein one momentum has an imaginary value, thereby amplifying the other momentum component. The underlying mechanism bears resemblance to plasmonic modes while distinctly lacking its inherent ohmic loss. **a**,**b**, Schematic, dispersion relation (**a**) and relationship between radial and angular wavevectors (**b**, blue curve) of the dielectric singular mode supported by a dielectric bowtie antenna. The electric field shows divergence as ρ approaches zero, which results from the divergent radial and angular wavevector components (referred to as ik_ρ and k_φ, where k_ρ and k_φ are real numbers). The red curve in (**b**), which is plotted for reference, shows the relationship between radial and angular wavevectors when both are real. **c**,**d**, Schematic, dispersion relation (**c**) and dispersion curve (**d**) of the plasmonic mode supported by a metal–dielectric interface (Methods). The highest accessible momentum is limited by the ohmic loss. k_x and ik_y are denoted as the momenta of the plasmonic mode in the propagating direction and transverse direction respectively. In **a**–**d**, k_0 represents the wavevector in free space and n represents the refractive index of the dielectric material in the corresponding structure.

subdiffraction-limited mode volume[45–49]. The uniqueness of this structure is attributed to a self-similar boundary condition effect, treating the dielectric bowtie nanoantenna as a continuously diminishing dielectric–air–dielectric, air–dielectric–air self-similar configuration where boundary conditions contribute to field enhancement at the nanoantenna's apices[45,46]. However, a fundamental explanation for the breaking of the diffraction limit in the structure is currently absent. Furthermore, relevant experimental studies are currently constrained to the construction of passive dielectric cavities.

In this work, we demonstrate a dielectric nanolaser with a subdiffraction-limited mode volume. Our approach involves integrating a dielectric bowtie nanoantenna within a twisted lattice nanocavity to construct the device. We find that the electric-field singularity at the apices of the dielectric bowtie nanoantenna originates from divergence of momentum, leading to a highly concentrated field (Fig. 1). Near the apices, the angular momentum component of the singularity is a real number, while the radial component is an imaginary number, both of equal magnitude. In close proximity to the apices, the absolute values of these two momenta diverge (Fig. 1a,b). Notably, the total momentum, comprising these two momenta, remains a finite small value determined by the dielectric constant of the material. This mechanism, reminiscent of the plasmonic mode but devoid of ohmic losses, involves one momentum being imaginary, contributing to the increase of the other momentum component (Fig. 1c,d). In experiments, we meticulously control the gap size at the apices of the bowtie nanoantenna through a two-step process involving etching and atomic layer deposition. This precision allows us to achieve a nanoantenna structure with a single-nanometre gap size. By combining the nanoantenna with a twisted lattice nanocavity to suppress its high radiation loss, we successfully realize a subdiffraction-limited singular dielectric nanolaser with feature size at the 1-nm scale.

Infinite singularity

To break the diffraction limit with a dielectric structure, we use a dielectric bowtie nanoantenna embedded within a twisted lattice nanocavity (Fig. 2). The nanoantenna comprises a pair of triangular dielectric nanoparticles positioned adjacent to each other, with their apices directed towards one another. The twisted lattice nanocavity[28,50] effectively confines the light field, restricting it to a diffraction-limited spot in the central region of the nanocavity where the bowtie nanoantenna is positioned. The bowtie nanoantenna serves to further confine the intensity of the light field at its apices. As the issue of electric-field divergence at metal or dielectric tips is well explored in electrostatics scenarios[51,52], our focus here lies in providing a solution within the realm of electromagnetic waves. Such a solution unveils the underlying physics of the strongly localized cavity eigenmode in the structure.

In the realm of electromagnetic waves, our analysis indicates the presence of an infinite singularity in the electric field at these points (see 'Theoretical analysis of infinite singularity' in Methods). In the proximity of the apices (where $k_0\rho \ll 1$, with k_0 being the free-space wavevector and ρ representing the distance from the apices), the solutions to the wave equation take the form $\mathbf{E} = \mathbf{E}_+ + \mathbf{E}_-$ in each region that has a uniform refractive index, where $\mathbf{E}$ represents the electric field and $\mathbf{E}_\pm = C_\pm(k_0\rho)^{-l}e^{\mp il\varphi}(\mathbf{e}_x \pm i\mathbf{e}_y)$. Here $C_\pm$ are constants, $\mathbf{e}_x$ and $\mathbf{e}_y$ denote the unit vectors along the x and y directions, respectively, φ represents the azimuth angle in cylinder coordination, l ($0 < l < 1$) represents topological charge, and higher-order small terms have been disregarded. To fulfil the periodic boundary condition, the integral of the phase change of the solved eigenmode along a circle enclosing the apices must be an integer. The non-integral value of topological charge l arises from angular discontinuities in the dielectric constant, leading to phase jumps at the boundaries between the dielectric and air (Extended Data Fig. 1). It is noteworthy that the magnitude of l must be less than 1 to preserve the physically allowed solution with infinite singularity.

As $-l < 0$, $\mathbf{E}_\pm$ become divergent as ρ approaches zero. This infinite singularity originates from the substantial radial and angular wavevector components (referred to as ik_ρ and k_φ, where k_ρ and k_φ are real numbers) within the eigenmode, even though the overall wavevector remains quite small, determined by the material's dielectric constant. On closer examination of the expression for $\mathbf{E}_\pm$, it becomes apparent that both ik_ρ and k_φ are position dependent. To delineate the position-dependent wavevectors, we introduce the expression $E(\rho, \varphi) \equiv e^{i\int \mathbf{k}\cdot d\mathbf{r}}$. Consequently, we can derive the position-dependent expressions for ik_ρ and k_φ of $\mathbf{E}_\pm$, yielding $ik_\rho = i\frac{l}{\rho}$ and $k_\varphi = \pm\frac{l}{\rho}$.

The dispersion relation for the eigenmode can be expressed through the wave equation as follows:

$$(ik_\rho)^2 + k_\varphi^2 - i\left(\frac{\partial}{\partial\rho} + \frac{1}{\rho}\right)(ik_\rho) - i\frac{1}{\rho}\frac{\partial}{\partial\varphi}k_\varphi = \left(\frac{n\omega}{c}\right)^2,$$

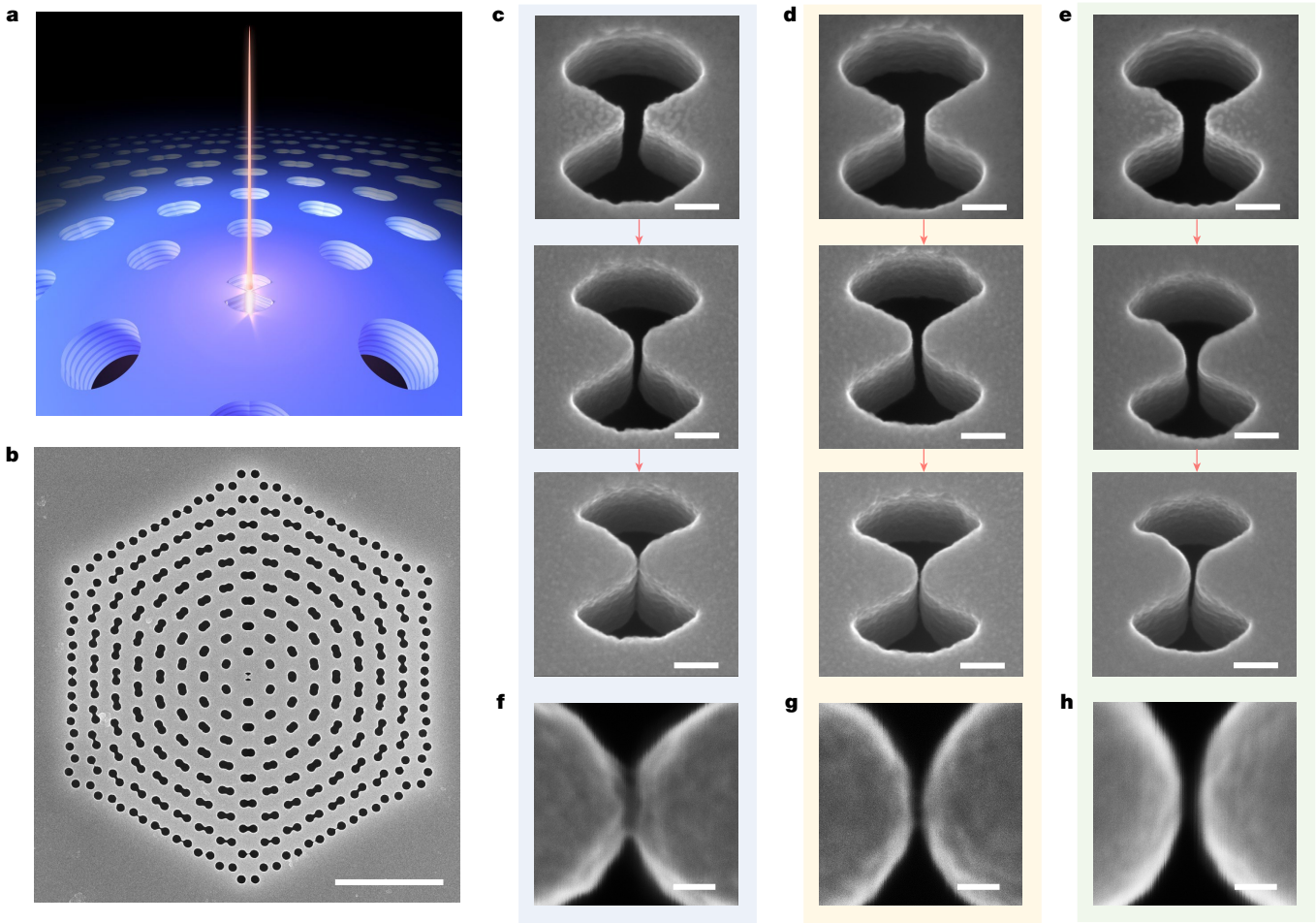

Fig. 2 | Fabrication of singular dielectric nanolasers featuring nanoantennas with atomic-scale gap sizes. a, Schematic of a singular dielectric nanolaser with atomic-scale field localization. **b**, SEM image depicting a singular dielectric nanolaser with a nanoantenna with an atomic-scale gap positioned at the centre of the cavity. **c**–**e**, Sequential perspective-view SEM images showing meticulous control over nanoantenna gap sizes in three singular dielectric nanolasers. In the first row, initial gap sizes are approximately 20 nm, with the gaps on the right slightly larger than those on the left. Following the first (SEM images shown in the second row) and second (SEM images shown in the third row) round of atomic layer deposition of TiO_2, gap sizes undergo progressive reduction. **f**–**h**, Enlarged top-view SEM images of the images from the third row of **c** (**f**), **d** (**g**) and **e** (**h**). The gap in the nanolaser shown in **f** is near closure, whereas those in nanolasers depicted in **g** and **h** are reduced to (1.7 ± 1.0) nm and (3.7 ± 1.2) nm respectively. Scale bars, 2 µm (**b**), 50 nm (**c**–**e**) and 10 nm (**f**–**h**).

where n represents the refractive index of the region described by the dispersion relation, ω represents the angular frequency and c represents the speed of light in vacuum.This dispersion relation is valid for the entire spatial domain. When ρ approaches zero, the magnitudes of $(ik_\rho)^2$ and k_φ^2 become significantly larger than all other terms. As ik_ρ is imaginary and k_φ is real, there is a mutual cancellation between the two terms $(ik_\rho)^2$ and k_φ^2. As k_ρ is much larger than the free-space wavevector as ρ approaches zero, the radial term $e^{-\int k_\rho d\rho}$ of $E(\rho,\varphi)$ causes the field to diminish to a very small magnitude over a distance substantially shorter than the free-space wavelength. This results in a strongly localized field near the singularity, with a linewidth that can be much smaller than 1 nm (Extended Data Fig. 1).

When $k_0\rho$ is no longer significantly smaller than 1, the mode with the diverging electric field at the apices starts showing magnetic-field components and outward energy flow (see 'Theoretical analysis of infinite singularity' in Methods). Consequently, the nanoantenna is unable to independently form a subdiffraction-limit mode. To overcome this limitation, we integrate it into a twisted lattice nanocavity. The synergistic combination of these elements not only realizes a subdiffraction-limit nanocavity with extremely small feature size but also imparts a high-quality factor inherited from the twisted lattice nanocavity.

Single-nanometre nanoantenna gap

We develop a two-step process involving etching and atomic layer deposition to fabricate the required dielectric bowtie nanoantenna with a single-nanometre gap embedded in a twisted lattice nanocavity (Fig. 2, 'Device fabrication' in Methods and Extended Data Fig. 2). The fabrication process begins with e-beam lithography, transferring the predefined pattern onto the e-beam resist. Subsequently, inductively coupled plasma etching shapes the desired nanostructure within a semiconductor membrane containing multiple quantum wells, with a thickness of 200 nm. A twisted angle of 3.89° exists between the two lattices, and the whole cavity's side length is approximately 4 µm. The bowtie gap, formed through this process, is typically about 20 nm.

Following this, we use the atomic layer deposition (ALD) method to achieve a conformal growth of a thin film of titanium dioxide (TiO_2) on the fabricated devices, providing precise control over the gap size (Fig. 2c–h and Extended Data Fig. 3). Three-dimensional full-wave simulation indicates a decrease in mode volume as the bowtie nanoantenna gap size is reduced by the ALD-deposited TiO_2 layer (Extended Data Fig. 4). Leveraging the atomic-level precision of conformal film deposition using ALD, our two-step process of etching

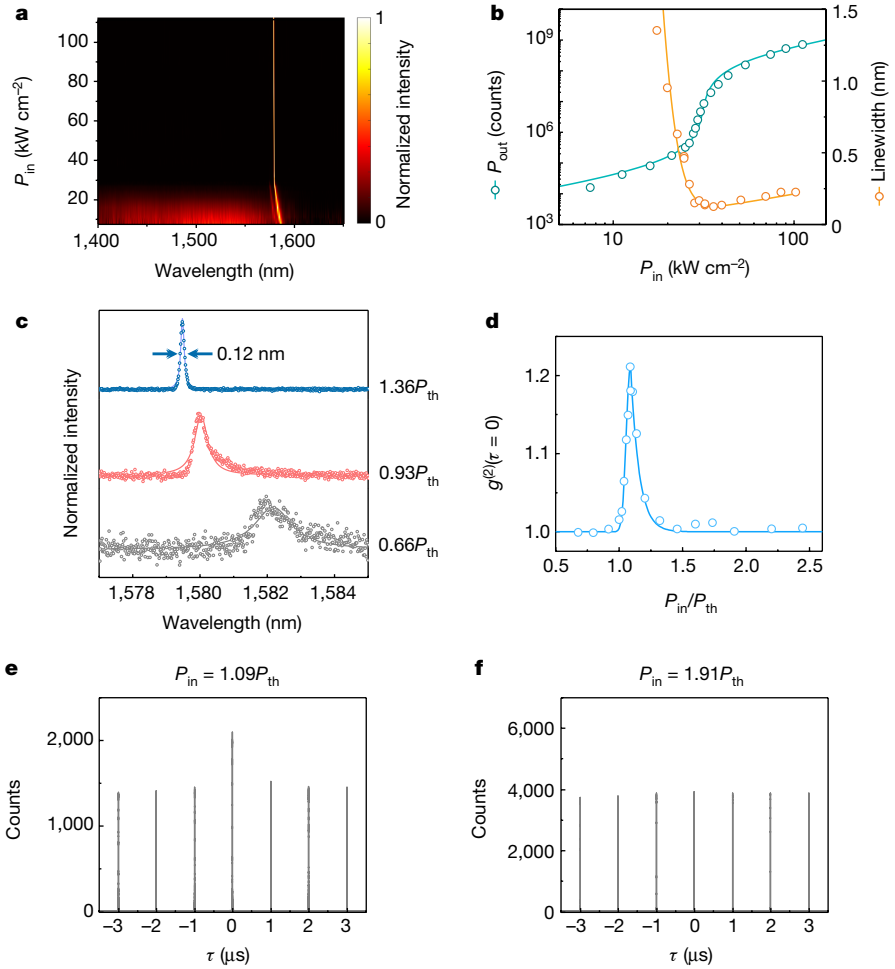

Fig. 3 | Lasing properties of a singular dielectric nanolaser. a, Normalized spectra at varied pump intensity (P_{in}), revealing a clear phase transition from spontaneous emission to lasing emission at a threshold (P_{th}) of approximately 26 kW cm^{-2}. **b**, Light–light curve in log–log scale (in green) and linewidth-evolution curve with pump power (in orange) of the lasing mode. P_{out} represents output power of the nanolaser. The circles represent the data and the lines denote the fitting. The fitting of the light–light curve results in a spontaneous emission coupling factor, β, of approximately 3.4×10^{-4}. **c**, Normalized emission spectra near the lasing threshold, demonstrating the linewidth narrowing of the lasing mode. The blueshift of the lasing peak with the increase of the pump power is because of the free-carrier dispersion effect. The circles represent the data and the lines illustrate the fitting. **d**, Second-order intensity correlation function $g^{(2)}(\tau = 0)$ of the nanolaser, showcasing super-Poissonian light characteristics ($g^{(2)}(\tau = 0) > 1$) around the lasing threshold. Upon surpassing the lasing threshold, emitted photons show coherence, shifting their statistics from super-Poissonian to Poissonian ($g^{(2)}(\tau = 0) = 1$). The circles denote the data and the line serves as a guide to the eye. **e**,**f**, $g^{(2)}(\tau)$ of the nanolaser at 1.09P_{th} (**e**) and 1.91P_{th} (**f**).

and atomic layer deposition enables us to achieve a bowtie gap size as small as a single nanometre.

The scanning electron microscopy (SEM) images depicted in Fig. 2c–h show the precise control achieved over gap sizes in three distinct devices. Following the initial etching step, the bowtie nanoantennas embedded within the twisted lattice nanocavities show gap sizes of approximately 20 nm (Fig. 2c–e, top panels). Subsequent to this, we utilize ALD to deposit TiO_2 onto the devices over two cycles (Fig. 2c–e, middle and bottom panels), progressively diminishing the gap sizes to near closure, measuring at (1.7 ± 1.0) nm and (3.7 ± 1.2) nm, respectively (Fig. 2f–h; the uncertainties are derived from fitting SEM image intensity profiles as discussed in the caption of Extended Data Fig. 5). This demonstrates a remarkable ability to finely modulate gap sizes within the nanostructures with precision and control. The singular dielectric nanolasers are then optically pumped at room temperature to obtain their lasing properties (Supplementary Fig. 1).

Lasing properties

We validate the lasing behaviour of singular dielectric nanolasers through an assessment of their nonlinear phase transition in the light–light curve, the linewidth-narrowing effect and the second-order intensity correlation function ($g^{(2)}(\tau)$ where τ is time delay). Figure 3a shows the normalized spectra at varied pump intensity of a singular dielectric nanolaser with gap size at the 1-nm scale, revealing the emergence of single-mode lasing with the increased pump power. Figure 3b shows the corresponding light–light curve and the cavity mode linewidth-evolution curve. The S-shaped log-scale light–light curve indicates the phase transition from spontaneous emission to stimulated emission. On the basis of the quantum threshold definition, the lasing threshold is set at 26 kW cm^{-2}. Beyond the threshold, the cavity mode's linewidth undergoes a rapid reduction. Figure 3c shows three spectra corresponding to pump powers below, near and above the lasing threshold, respectively. These spectra clearly illustrate the linewidth-narrowing effect and the dominance of lasing emission over spontaneous emission beyond the lasing threshold. The highest lasing quality factor obtained from the spectra is 13,200. With the spatial overlap between the cavity mode and the gain medium largely unaffected by variations in the thickness of the ALD-deposited TiO_2 layer (Extended Data Fig. 4d), the lasing threshold and linewidth essentially remain constant with varied TiO_2 layer thickness (Supplementary Fig. 2).

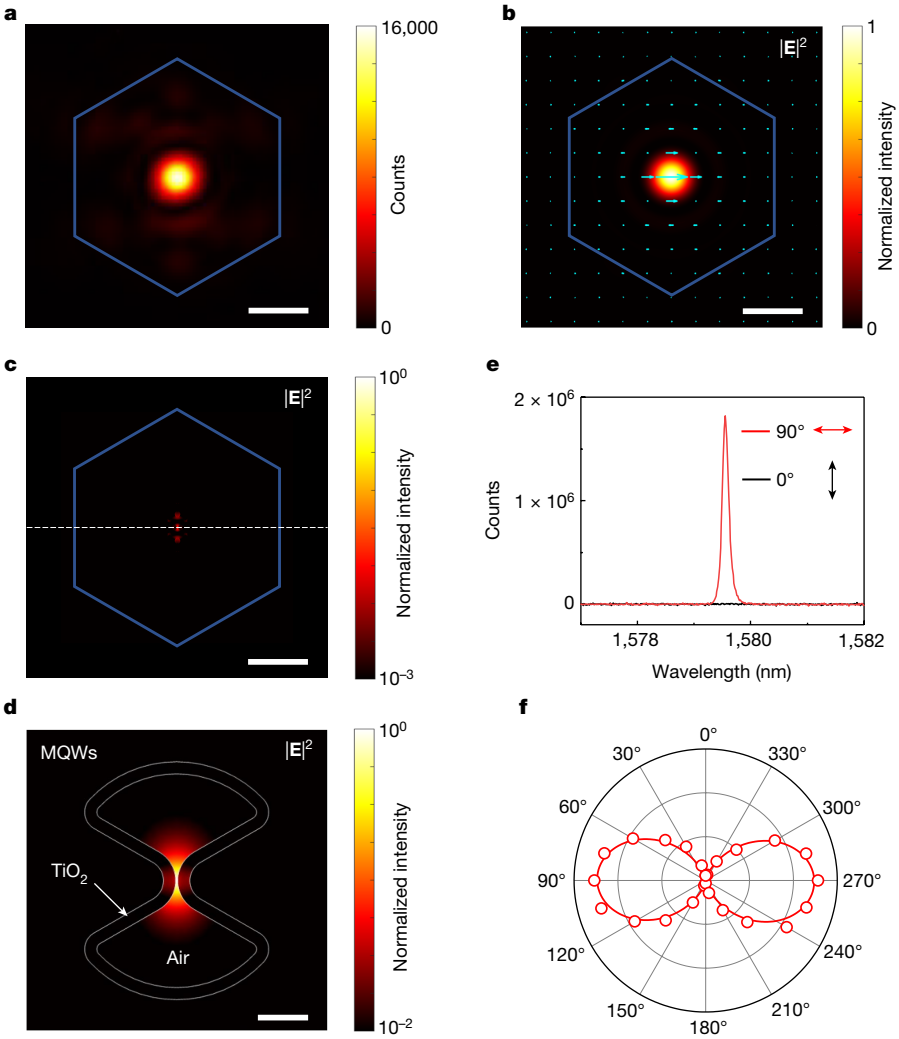

Fig. 4 | Mode properties of the singular dielectric nanolaser. a, Experimental lasing emission pattern of the singular dielectric nanolaser. **b**, Three-dimensional full-wave simulated emission pattern of the lasing cavity mode, with superimposed arrows indicating polarization directions. **c**, Three-dimensional full-wave simulated electric-field pattern of the lasing cavity mode represented on a logarithmic scale. The blue hexagons in **a**–**c** indicate the edge of the nanolaser. The differences between **b** and **c** arise from the spatial resolution of the lasing emission collective system of approximately 1 µm. **d**, Enlarged electrical-field pattern depicted in **c**, highlighting the atomic-scale field localization at the centre of the nanoantenna. MQWs, multiple quantum wells. **e**, Experimental polarization-resolved lasing emission spectra, showcasing experimental observations aligning closely with simulated polarization directions illustrated in **b**. The arrows represent polarization directions of 90° (red) and 0° (black). **f**, Experimental lasing emission intensity plotted as a function of the polarization angle. Scale bars, 2 µm (**a**–**c**) and 40 nm (**d**).

Lasing is further affirmed through the characterization of the singular dielectric nanolaser using $g^{(2)}(\tau)$ (Fig. 3d–f). In proximity to the lasing threshold, the emitted photons show super-Poissonian characteristics ($g^{(2)}(\tau = 0) > 1$). Above the threshold, the photon emission statistics transition from super-Poissonian to Poissonian, indicating coherent light emission ($g^{(2)}(\tau = 0) = 1$). Decreasing the pump power below the threshold results in a decline in measured values for $g^{(2)}(\tau = 0)$, attributed to a reduction in the coherence length of spontaneous emission approaching the temporal resolution limit (100 ps) imposed by our measurement set-up. Regarding the emission rate, the strong localized field results in an accelerated emission rate, corresponding to a Purcell factor of 58 (Supplementary Fig. 3). In Extended Data Table 1, we provide a comparison of key laser merits, including threshold, lasing quality factor and mode volume, with other state-of-the-art microscale lasers.

Lasing-mode properties

In Fig. 4a, the lasing emission pattern of the singular dielectric nanolaser is depicted, demonstrating a close resemblance to the three-dimensional full-wave simulated counterpart shown in Fig. 4b. The spontaneous emission pattern, in contrast, is determined by the pump beam (Supplementary Fig. 4). Figure 4c,d shows the simulated electric-field pattern of the cavity mode on a log scale, which illustrates the strong field localization at the centre of the nanoantenna. Figure 4e,f shows the polarization-resolved lasing emission spectra alongside the normalized lasing emission intensity as a function of the polarization angle. Notably, the observed mode polarization aligns well with the simulated polarization direction shown as arrows in Fig. 4b. On the basis of three-dimensional full-wave simulation, the lasing mode demonstrates an ultrasmall mode volume of approximately $0.0005\,\lambda^3$, where λ is free-space wavelength. This mode volume is less than one-sixth of the optical diffraction limit of $(\lambda/2n)^3$. Owing to the ultrasmall mode volume, the device shows a large divergent angle (Supplementary Fig. 5). Highly directional emission can be realized by coupling an array of the nanolasers[36].

We have calculated the mode volumes of nanocavities, considering potential defects such as tilt angles, surface roughness and point defects. Our findings indicate that tilt angles and surface roughness

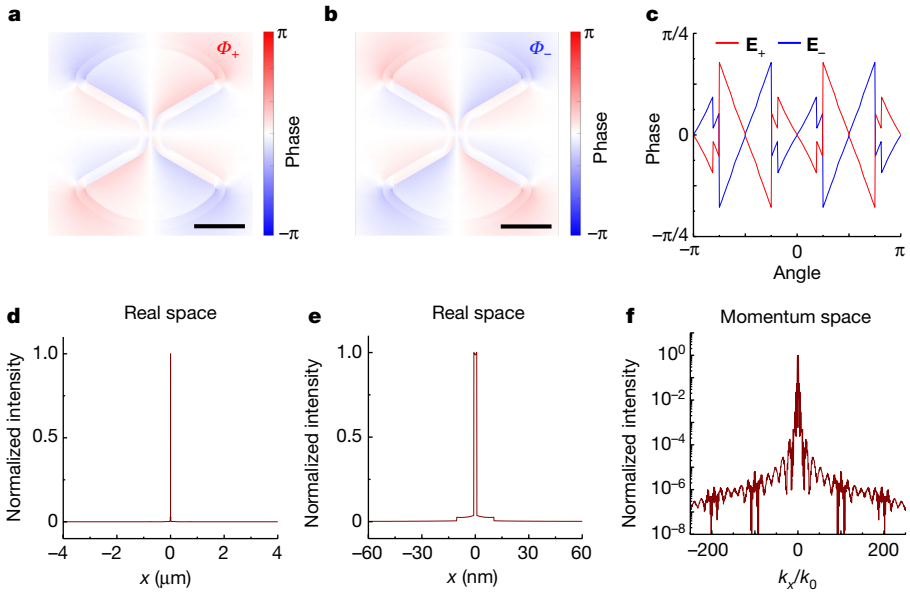

Fig. 5 | Non-integral topological charge and the atomic-scale localized optical field. a,**b**, Simulated phases Φ_+ (**a**) and Φ_- (**b**) of the electric-field components $\mathbf{E}_\pm$ obtained from three-dimensional full-wave simulated near-field pattern represented as $\mathbf{E}_\pm = E_\pm(\mathbf{e}_x \pm i\mathbf{e}_y)$, where $E_\pm = |E_\pm| e^{i\Phi_\pm}$. The non-integral value of the topological charge l of 0.63 stems from angular discontinuities in the dielectric constant, inducing phase jumps at the boundaries between the dielectric and air. Scale bars, 50 nm. **c**, Simulated phase changes of $\mathbf{E}_\pm$ along a circle enclosing the apices. The integral of the phase change along the circle for both $\mathbf{E}_\pm$ yields an integer value of zero, thereby satisfying the periodic boundary condition. **d**,**e**, Simulated intensity profile (**d**) and the zoomed-in profile (**e**) along the dashed line in Fig. 4c, highlighting the atomic-scale field localization enabled by the electric-field infinite singularity. **f**, Simulated intensity profile in momentum space along the same direction in **d**. The atomic-scale localized field corresponds to a large wavevector distribution spanning over $100k_0$.

do not substantially affect the mode volume (Extended Data Figs. 6 and 7). Atomic-scale point defects can further reduce the mode volume to as small as $0.0001\lambda^3$ (Extended Data Fig. 6).

To further substantiate the profound impact of the bowtie nanoantenna on cavity modes, we preserve the overall moiré structure while altering the orientation of the embedded nanoantennas. Both the three-dimensional full-wave simulation and experimental findings demonstrate that the polarization direction of the lasing mode adjusts with the nanoantenna's rotation angle (Extended Data Fig. 8).

Figure 5a,b depicts the phases ($\Phi_\pm$) of the electric-field components $\mathbf{E}_+$ and $\mathbf{E}_-$ derived from three-dimensional full-wave simulated cavity mode, represented as $\mathbf{E}_\pm = E_\pm(\mathbf{e}_x \pm i\mathbf{e}_y)$, where $E_\pm = |E_\pm|\ e^{i\Phi_\pm}$. Phase jumps at the boundaries between the dielectric and air are clearly presented, which results in the non-integral topological charge l of 0.63. Figure 5c illustrates the phase changes of $\mathbf{E}_\pm$ along a circle enclosing the apices. The integral of the phase change along the circle for both $\mathbf{E}_\pm$ yields an integer value of zero, satisfying the periodic boundary condition. Figure 5d,e depicts the intensity profile and a magnified view along the dashed line in Fig. 4c, respectively, highlighting the atomic-scale field localization. Log-scale profiles are presented in Extended Data Fig. 9a,b. Figure 5f shows the intensity profile in momentum space along the same direction (the dashed line in Extended Data Fig. 9c), revealing atomic-scale localized field corresponding to a broad wavevector distribution spanning over $100k_0$.

Summary

In this work, we have proposed and demonstrated a singular dielectric nanolaser with a subdiffraction-limited mode volume. By integrating a dielectric bowtie nanoantenna into the centre of a twisted lattice nanocavity, the device achieves an unprecedented small feature size at the 1-nm scale. The fabrication process involves a two-step method of etching and atomic layer deposition to create a dielectric bowtie nanoantenna with a single-nanometre gap. The nanoantenna's unique ability to support an infinite singularity of electric field at its apices, derived from Maxwell's equations, enables extreme field localization at the atomic scale. The study uncovers the mechanism behind this phenomenon, where one momentum component is imaginary, resembling a plasmonic mode but without metal losses. Experimental control of the gap size at the bowtie tip, combined with a twisted lattice nanocavity to suppress radiation losses, results in the realization of a subdiffraction-limited singular dielectric nanolaser with remarkable potential for ultra-precise measurements, super-resolution imaging, ultra-efficient computing and communication, and the exploration of light–matter interactions in extreme optical field localization.

Online content

Any methods, additional references, Nature Portfolio reporting summaries, source data, extended data, supplementary information, acknowledgements, peer review information; details of author contributions and competing interests; and statements of data and code availability are available at https://doi.org/10.1038/s41586-024-07674-9.

1. Shim, H., Monticone, F. & Miller, O. D. Fundamental limits to the refractive index of transparent optical materials. *Adv. Mater.* **33**, 2103946 (2021).
2. Khurgin, J. B. Expanding the photonic palette: exploring high index materials. *ACS Photon.* **9**, 743–751 (2022).
3. Schuller, J. A. et al. Plasmonics for extreme light concentration and manipulation. *Nat. Mater.* **9**, 193–204 (2010).
4. Gramotnev, D. K. & Bozhevolnyi, S. I. Plasmonics beyond the diffraction limit. *Nat. Photon.* **4**, 83–91 (2010).
5. Kauranen, M. & Zayats, A. V. Nonlinear plasmonics. *Nat. Photon.* **6**, 737–748 (2012).
6. Tame, M. S. et al. Quantum plasmonics. *Nat. Phys.* **9**, 329–340 (2013).
7. Khurgin, J. B. Ultimate limit of field confinement by surface plasmon polaritons. *Faraday Discuss.* **178**, 109–122 (2015).
8. Khurgin, J. B. How to deal with the loss in plasmonics and metamaterials. *Nat. Nanotechnol.* **10**, 2–6 (2015).
9. Maiman, T. H. Stimulated optical radiation in ruby. *Nature* **187**, 493–494 (1960).
10. Weiss, R., Barish, B. C. & Thorne K. S. Press release: The Nobel Prize in Physics 2017. *The Nobel Prize* https://www.nobelprize.org/prizes/physics/2017/press-release/ (2017).

11. Agostini, P., Krausz, F. & L'Huillier, A. Press release: The Nobel Prize in Physics 2023. *The Nobel Prize* https://www.nobelprize.org/prizes/physics/2023/press-release/ (2023).
12. NASA Deep Space Optical Communications (DSOC). *NASA* https://www.nasa.gov/mission/deep-space-optical-communications-dsoc/ (2023).
13. Yokoyama, H. & Brorson, S. D. Rate equation analysis of microcavity lasers. *J. Appl. Phys.* **66**, 4801–4805 (1989).
14. Björk, G. & Yamamoto, Y. Analysis of semiconductor microcavity lasers using rate equations. *IEEE J. Quantum Electron.* **27**, 2386–2396 (1991).
15. Berini, P. & De Leon, I. Surface plasmon–polariton amplifiers and lasers. *Nat. Photon.* **6**, 16–24 (2012).
16. Hill, M. T. & Gather, M. C. Advanced in small lasers. *Nat. Photon.* **8**, 908–918 (2014).
17. Eaton, S. W., Fu, A., Wong, A. B., Ning, C. Z. & Yang, P. Semiconductor nanowire lasers. *Nat. Rev. Mater.* **1**, 16028 (2016).
18. Ma, R. M. & Oulton, R. F. Applications of nanolasers. *Nat. Nanotechnol.* **14**, 12–22 (2019).
19. Azzam, S. I. et al. Ten years of spasers and plasmonic nanolasers. *Light Sci. Appl.* **9**, 90 (2020).
20. Bandres, M. A. et al. Topological insulator laser: experiments. *Science* **359**, eaar4005 (2018).
21. Ha, S. T. et al. Directional lasing in resonant semiconductor nanoantenna arrays. *Nat. Nanotechnol.* **13**, 1042–1047 (2018).
22. Yoshida, M. et al. Double-lattice photonic-crystal resonators enabling high-brightness semiconductor lasers with symmetric narrow-divergence beams. *Nat. Mater.* **18**, 121–128 (2019).
23. Carlon Zambon, N. et al. Optically controlling the emission chirality of microlasers. *Nat. Photon.* **13**, 283–288 (2019).
24. Zeng, Y. et al. Electrically pumped topological laser with valley edge modes. *Nature* **578**, 246–250 (2020).
25. Shao, Z. K. et al. A high-performance topological bulk laser based on band-inversion-induced reflection. *Nat. Nanotechnol.* **15**, 67–72 (2020).
26. Yang, Z. Q., Shao, Z. K., Chen, H. Z., Mao, X. R. & Ma, R. M. Spin-momentum-locked edge mode for topological vortex lasing. *Phys. Rev. Lett.* **125**, 013903 (2020).
27. Huang, C. et al. Ultrafast control of vortex microlasers. *Science* **367**, 1018–1021 (2020).
28. Mao, X. R., Shao, Z. K., Luan, H. Y., Wang, S. L. & Ma, R. M. Magic-angle lasers in nanostructured moiré superlattice. *Nat. Nanotechnol.* **16**, 1099–1105 (2021).
29. Dikopoltsev, A. et al. Topological insulator vertical-cavity laser array. *Science* **373**, 1514–1517 (2021).
30. Wu, H. et al. Photonic nanolaser with extreme optical field confinement. *Phys. Rev. Lett.* **129**, 013902 (2022).
31. Contractor, R. et al. Scalable single-mode surface-emitting laser via open-Dirac singularities. *Nature* **608**, 692–698 (2022).
32. Zhang, Z. et al. Spin–orbit microlaser emitting in a four-dimensional Hilbert space. *Nature* **612**, 246–251 (2022).
33. Yang, L., Li, G., Gao, X. & Lu, L. Topological-cavity surface-emitting laser. *Nat. Photon.* **16**, 279–283 (2022).
34. Chen, Y. et al. Compact spin-valley-locked perovskite emission. *Nat. Mater.* **22**, 1065–1070 (2023).
35. Hwang, M. S. et al. Vortex nanolaser based on a photonic disclination cavity. *Nat. Photon.* **18**, 286–293 (2024).
36. Luan, H. Y., Ouyang, Y. H., Zhao, Z. W., Mao, W. Z. & Ma, R. M. Reconfigurable moiré nanolaser arrays with phase synchronization. *Nature* **624**, 282–288 (2023).
37. Bergman, D. J. & Stockman, M. I. Surface plasmon amplification by stimulated emission of radiation: quantum generation of coherent surface plasmons in nanosystems. *Phys. Rev. Lett.* **90**, 027402 (2003).
38. Zhong, X. L. & Li, Z. Y. All-analytical semiclassical theory of spaser performance in a plasmonic nanocavity. *Phys. Rev. B* **88**, 085101 (2013).
39. Hess, O. & Tsakmakidis, K. L. Metamaterials with quantum gain. *Science* **339**, 654–655 (2013).
40. Bian, Y. S. & Gong, Q. H. Bow-tie hybrid plasmonic waveguides. *J. Lightwave Technol.* **32**, 4504–4509 (2014).
41. Chipouline, A. & Küppers, F. Analytical qualitative modeling of passive and active metamaterials. *J. Opt. Soc. Am. B* **34**, 1597–1623 (2017).
42. Oulton, R. F. et al. Plasmon lasers at deep subwavelength scale. *Nature* **461**, 629–632 (2009).
43. Hill, M. T. et al. Lasing in metal–insulator–metal sub-wavelength plasmonic waveguides. *Opt. Express* **17**, 11107–11112 (2009).
44. Noginov, M. A. et al. Demonstration of a spaser-based nanolaser. *Nature* **460**, 1110–1112 (2009).
45. Hu, S. & Weiss, S. M. Design of photonic crystal cavities for extreme light concentration. *ACS Photon.* **3**, 1647–1653 (2016).
46. Choi, H., Heuck, M. & Englund, D. Self-similar nanocavity design with ultrasmall mode volume for single-photon nonlinearities. *Phys. Rev. Lett.* **118**, 223605 (2017).
47. Hu, S. et al. Experimental realization of deep-subwavelength confinement in dielectric optical resonators. *Sci. Adv.* **4**, eaat2355 (2018).
48. Albrechtsen, M. et al. Nanometer-scale photon confinement in topology-optimized dielectric cavities. *Nat. Commun.* **13**, 6281 (2022).
49. Babar, A. N. et al. Self-assembled photonic cavities with atomic-scale confinement. *Nature* **624**, 57–63 (2023).
50. Ma, R. M. et al. Twisted lattice nanocavity with theoretical quality factor exceeding 200 billion. *Fundam. Res.* **3**, 537–543 (2023).
51. Jackson, J. D. *Classical Electrodynamics* (Wiley, 1999).
52. Andersen, J. & Solodukhov, V. Field behavior near a dielectric wedge. *IEEE Trans. Antennas Propag.* **26**, 598–602 (1978).

Methods

Theoretical analysis of infinite singularity

Electric-field singularity at the apices of the dielectric bowtie nanoantenna originates from divergence of momentum, leading to a highly concentrated field (Extended Data Fig. 1). In the following, we theoretically derive the expression of this singularity from Maxwell's equations.

We consider transverse-electric eigenmodes of a dielectric bowtie nanoantenna with a negligible gap between its two apices (Extended Data Fig. 1a). Each dielectric triangular unit comprising the nanoantenna has a tip angle of θ. Consequently, the entire structure shows a refractive index distribution $n(\rho, \varphi)$ as

$$n(\rho,\varphi)=\begin{cases} n\ (n>1) & \left(-\frac{\theta}{2}\le\varphi\le\frac{\theta}{2}\ \text{or}\ \pi-\frac{\theta}{2}\le\varphi\le\pi+\frac{\theta}{2}\right) \\ 1 & \left(-\pi+\frac{\theta}{2}<\varphi<-\frac{\theta}{2}\ \text{or}\ \frac{\theta}{2}<\varphi<\pi-\frac{\theta}{2}\right) \end{cases}. \tag{1}$$

In each region that has a uniform refractive index, Maxwell's equations can be written as

$$\begin{cases} \nabla\times\mathbf{E}=-\mu_0\dfrac{\partial\mathbf{H}}{\partial t} \\ \nabla\times\mathbf{H}=n^2\varepsilon_0\dfrac{\partial\mathbf{E}}{\partial t} \\ \nabla\cdot\mathbf{E}=0 \\ \nabla\cdot\mathbf{H}=0 \end{cases}. \tag{2}$$

In equation (2), $\mathbf{E}$ and $\mathbf{H}$ are electric and magnetic fields of the eigenmodes respectively, ε_0 and μ_0 are permittivity and permeability of vacuum respectively, and t represents time. The eigenmodes of the structure under consideration are those that do not propagate along the z direction, necessitating a wavevector with zero z component. Subsequently, we solve the wave equation in cylindrical coordinates ρ, φ, z, where the time-dependent term is represented as $e^{-i\omega t}$ and the electric-field eigenmode of $\mathbf{E}$ is decomposed into its x, y, z components E_j (where $j = x, y, z$). The wave equation is

$$\begin{cases} \left(\dfrac{\partial^2}{\partial\rho^2}+\dfrac{1}{\rho}\dfrac{\partial}{\partial\rho}\right)E_j+\dfrac{1}{\rho^2}\dfrac{\partial^2}{\partial\varphi^2}E_j+\left(\dfrac{n\omega}{c}\right)^2E_j=0,\ (j=x,y,z) \\ \left(\dfrac{\partial E_x}{\partial\rho}+\dfrac{1}{\rho}\dfrac{\partial E_y}{\partial\varphi}\right)\cos\varphi+\left(\dfrac{\partial E_y}{\partial\rho}-\dfrac{1}{\rho}\dfrac{\partial E_x}{\partial\varphi}\right)\sin\varphi=0 \end{cases}. \tag{3}$$

The eigenmode with an electric-field singularity at the apices of the dielectric bowtie nanoantenna is obtained by solving equation (3). Within the range of $k_0\rho \ll 1$ ($k_0 = \omega/c$ represents the free-space wavevector), the higher-order small terms of the electric field can be disregarded, and the eigenmodes $\mathbf{E}$ and $\mathbf{H}$ can be described as follows:

$$E_x=\begin{cases} \alpha C(k_0\rho)^{-l}\cos[l\varphi] & \left(-\frac{\theta}{2}\le\varphi\le\frac{\theta}{2}\right) \\ \alpha C(k_0\rho)^{-l}\cos[l(\pi-\varphi)] & \left(\pi-\frac{\theta}{2}\le\varphi\le\pi+\frac{\theta}{2}\right) \\ C(k_0\rho)^{-l}\cos\left[l\left(\frac{\pi}{2}+\varphi\right)\right] & \left(-\pi+\frac{\theta}{2}<\varphi<-\frac{\theta}{2}\right) \\ C(k_0\rho)^{-l}\cos\left[l\left(\frac{\pi}{2}-\varphi\right)\right] & \left(\frac{\theta}{2}<\varphi<\pi-\frac{\theta}{2}\right) \end{cases}$$

$$E_y=\begin{cases} \alpha C(k_0\rho)^{-l}\sin[l\varphi] & \left(-\frac{\theta}{2}\le\varphi\le\frac{\theta}{2}\right) \\ -\alpha C(k_0\rho)^{-l}\sin[l(\pi-\varphi)] & \left(\pi-\frac{\theta}{2}\le\varphi\le\pi+\frac{\theta}{2}\right) \\ C(k_0\rho)^{-l}\sin\left[l\left(\frac{\pi}{2}+\varphi\right)\right] & \left(-\pi+\frac{\theta}{2}<\varphi<-\frac{\theta}{2}\right) \\ -C(k_0\rho)^{-l}\sin\left[l\left(\frac{\pi}{2}-\varphi\right)\right] & \left(\frac{\theta}{2}<\varphi<\pi-\frac{\theta}{2}\right) \end{cases}, \tag{4}$$

$$E_z=0$$

$$H_x=H_y=H_z=0$$

where C is a normalized constant, $\alpha=\dfrac{\sin\left[(1-l)\frac{\pi-\theta}{2}\right]}{\cos\left[(1-l)\frac{\theta}{2}\right]}$ and the parameter l is determined by the following equation:

$$\tan\left[(1-l)\frac{\pi-\theta}{2}\right]\tan\left[(1-l)\frac{\theta}{2}\right]=\frac{1}{n^2},\ 0<l<1. \tag{5}$$

The solved eigenmode $\mathbf{E}$ is a standing mode that can be decomposed into travelling modes with the same amplitude but opposite non-integral orbit angular momenta of $\mp l$ and opposite spin angular momenta of ± 1.

$$\begin{aligned} &\mathbf{E}=\mathbf{E}_+ + \mathbf{E}_-, \\ &\begin{cases} \mathbf{E}_+ = C_+(k_0\rho)^{-l}e^{-il\varphi}(\mathbf{e}_x+i\mathbf{e}_y) \\ \mathbf{E}_- = C_-(k_0\rho)^{-l}e^{il\varphi}(\mathbf{e}_x-i\mathbf{e}_y) \end{cases}, \end{aligned} \tag{6}$$

where $(\mathbf{e}_x \pm i\mathbf{e}_y)$ represent electric fields with spin angular momenta of ± 1, $C_\pm$ are normalized constants, and $|C_+| = |C_-|$.

To describe position varied wavevectors $\mathbf{k}^j(\rho, \varphi)$ of $E_j(\rho, \varphi)$, we can use the expression of

$$E_j(\rho,\varphi)\equiv e^{i\int \mathbf{k}^j(\rho,\varphi)\cdot d\mathbf{r}}, \tag{7}$$

where $\mathbf{r}$ is position vector. The equation (7) is equivalent to

$$\mathbf{k}^j(\rho,\varphi)E_j(\rho,\varphi)=-i\nabla E_j(\rho,\varphi). \tag{8}$$

Using the expression given in equation (7) and the wave equation shown in equation (3), we can obtain the dispersion relation of

$$[ik_\rho(\rho,\varphi)]^2+k_\varphi^2(\rho,\varphi)-i\left(\frac{\partial}{\partial\rho}+\frac{1}{\rho}\right)[ik_\rho(\rho,\varphi)]-i\frac{1}{\rho}\frac{\partial}{\partial\varphi}k_\varphi(\rho,\varphi)=\left(\frac{n\omega}{c}\right)^2, \tag{9}$$

where $ik_\rho(\rho, \varphi)$ and $k_\varphi(\rho, \varphi)$ are the radial and angular wavevector components of $\mathbf{k}^j(\rho, \varphi)$, respectively.

Using the expression given in equation (8) and the eigenmode shown in equation (6), we can obtain $\mathbf{k}^j(\rho,\varphi)=\mathbf{k}(\rho,\varphi)\equiv ik_\rho\mathbf{e}_\rho+k_\varphi\mathbf{e}_\varphi$ $(j=x,y)$, $ik_\rho=i\frac{l}{\rho}$ and $k_\varphi=\pm\frac{l}{\rho}$.

As ρ approaches zero, the magnitudes of $(ik_\rho)^2$ and k_φ^2 in the dispersion relation shown in equation (9) are significantly larger than all other terms.

When the higher-order small terms need to be considered—specifically when $k_0\rho$ is not significantly smaller than 1—we derive the following expressions of the magnetic field of the infinite singularity: $H_x = H_y = 0$, $H_z=-i\sqrt{\frac{\varepsilon_0}{\mu_0}}(k_0\rho)^{-l+1}g(\varphi)$. For the infinite singular mode, where $0 < l < 1$, the radial term $(k_0\rho)^{-l+1}$ indicates that H_z approaches zero as $k_0\rho \ll 1$. When $k_0\rho$ is no longer significantly smaller than 1, H_z no longer approaches 0, leading to outward energy flow from the singularity. This is why dielectric nanoantennas alone are unable to support subdiffraction-limit modes.

To achieve the formation of a localized field that surpasses the diffraction limit in a pure dielectric structure, it is crucial that the topological charge (l) takes on a non-integer value. The concept of topological charge essentially describes the rate of phase change around a singularity. The rapid phase shift encircling the singularity corresponds to an effective large wavevector, which is key to breaking the diffraction limit. Through theoretical analyses and corroborated by full-wave simulations, we have arrived at the following conclusions. (1) When $l = 0$, the lack of an infinite singularity prevents the formation of a localized field capable of breaking the diffraction limit. (2) At $|l| \ge 1$, although solutions with infinite singularities exist, these solutions are not physically allowable. This is because, at the singularity, the solution required that material properties differ from that given in

the system. (3) For non-integer values of $|l|$ ranging between 0 and 1, a physically allowed infinite singularity arises, enabling the formation of a localized field capable of breaking the diffraction limit within pure dielectric structures.

Device fabrication

We fabricate the singular dielectric nanolaser using a semiconductor membrane composed of InGaAsP multiple quantum wells with a thickness of 200 nm (Extended Data Fig. 2). A single pattern file incorporating two sets of nanoholes with a predetermined twisted angle is designed and adjusted during the computer aided design (CAD) pattern drawing process, with the central hole being replaced by a bowtie nanoantenna. Subsequently, e-beam lithography is used to transfer the designed pattern onto the e-beam resist layer, completing the initial transfer process. Following this, the inductively coupled plasma etching technique is utilized to first transfer the pattern into the silicon dioxide mask layer and then the multiple quantum well layers. After these steps, diluted hydrochloric acid is applied to etch the InP substrate, resulting in the formation of the suspended membrane. Finally, ALD is utilized to deposit a high-conformal TiO_2 dielectric layer on the singular dielectric nanolasers, ensuring precise control over the gap width of the bowtie nanoantenna. The lattice constant of the employed triangular lattices is 465 nm, with nanoholes having a diameter of 170 nm. The cavity's side length is 3.955 μm.

Full-wave simulation

We simulate the eigenmodes of singular dielectric nanolaser cavities through three-dimensional full-wave simulations using the finite-element method. These simulations yield the full properties of the desired cavity mode, which include field distributions, quality factors and mode volumes. Within the simulation, the refractive indices of the semiconductor membrane and the TiO_2 layer are set to 3.43 and 2.28, respectively. For the calculation of plasmonic dispersion shown in Fig. 1d, we use a silver/dielectric interface, where the refractive index of silver is adopted from ref. 53, and that of the dielectric is set as 3.43. Ohmic loss results in limited propagation length and a corresponding broad momentum distribution. The mode volume is calculated using the formula: $V = \frac{\int \varepsilon(\mathbf{r})|\mathbf{E}(\mathbf{r})|^2 \mathrm{d}^3\mathbf{r}}{\max[\varepsilon(\mathbf{r})|\mathbf{E}(\mathbf{r})|^2]}$, where $\varepsilon(\mathbf{r})$ represents the position-dependent permittivity of the simulated structure. The quality factor is determined by $Q = (\mathrm{Re}[f])/(2\mathrm{Im}[f])$, where $\mathrm{Re}[f]$ and $\mathrm{Im}[f]$ denote the real and imaginary parts of the eigenfrequency of a simulated cavity eigenmode, respectively. The device presented in the study shows a twist angle of 3.89°, resulting in a cold cavity quality factor of 5,700. Higher quality factors can be achieved by reducing the twist angle[50] and fine-tuning the dimensions of the embedded bowtie antenna.

Optical characterization

We utilize a pulsed laser to excite the device under ambient temperature (wavelength 1,064 nm; pulse width 5 ns; repetition rate 12 kHz; Supplementary Fig. 1). Characterization of the emission properties of the nanolaser is carried out using a home-built microscopy system integrated with a near-infrared charge-coupled device and spectrometer. Both the excitation and the emission beams are collected by a shared objective lens (×100, numerical aperture 0.82). The spectrometer has a resolution of approximately 0.04 nm. For the evaluation of the second-order intensity correlation function $g^{(2)}(\tau)$, we employ a Hanbury-Brown and Twiss experimental set-up. This set-up utilizes a pulsed laser with a 1-MHz repetition rate as the pump source (wavelength 1,064 nm; pulse width 0.1 ns) and two superconducting nanowire single-photon detectors for correlating detection.

Data availability

We declare that the data supporting the findings of this study are available within the paper.

53. Johnson, P. B. & Christy, R. W. Optical constants of the noble metals. *Phys. Rev. B* **6**, 4370–4379 (1972).

Acknowledgements This work is supported by the National Natural Science Foundation of China (grant numbers 12225402, 62321004 and 92250302), the national Key R&D Program of China (grant numbers 2022YFA1404700 and 2018YFA0704401), the Beijing Natural Science Foundation (Z180011) and the New Cornerstone Science Foundation through the XPLORER PRIZE. We thank Peking Nanofab and National Center for Nanoscience and Technology for fabrication assistance.

Author contributions R.-M.M. conceived the concept and supervised the project. Y.-H.O., H.-Y.L. and W.-Z.M. performed the optical characterization. H.-Y.L. carried out the theoretical analysis. Z.-W.Z. fabricated the devices. H.-Y.L. and Y.-H.O. conducted the numerical simulations. R.-M.M., H.-Y.L. and Y.-H.O. did the data analysis. R.-M.M. wrote the paper.

Competing interests The authors declare no competing interests.

Additional information
Supplementary information The online version contains supplementary material available at https://doi.org/10.1038/s41586-024-07674-9.
Correspondence and requests for materials should be addressed to Ren-Min Ma.
Peer review information *Nature* thanks the anonymous reviewers for their contribution to the peer review of this work.

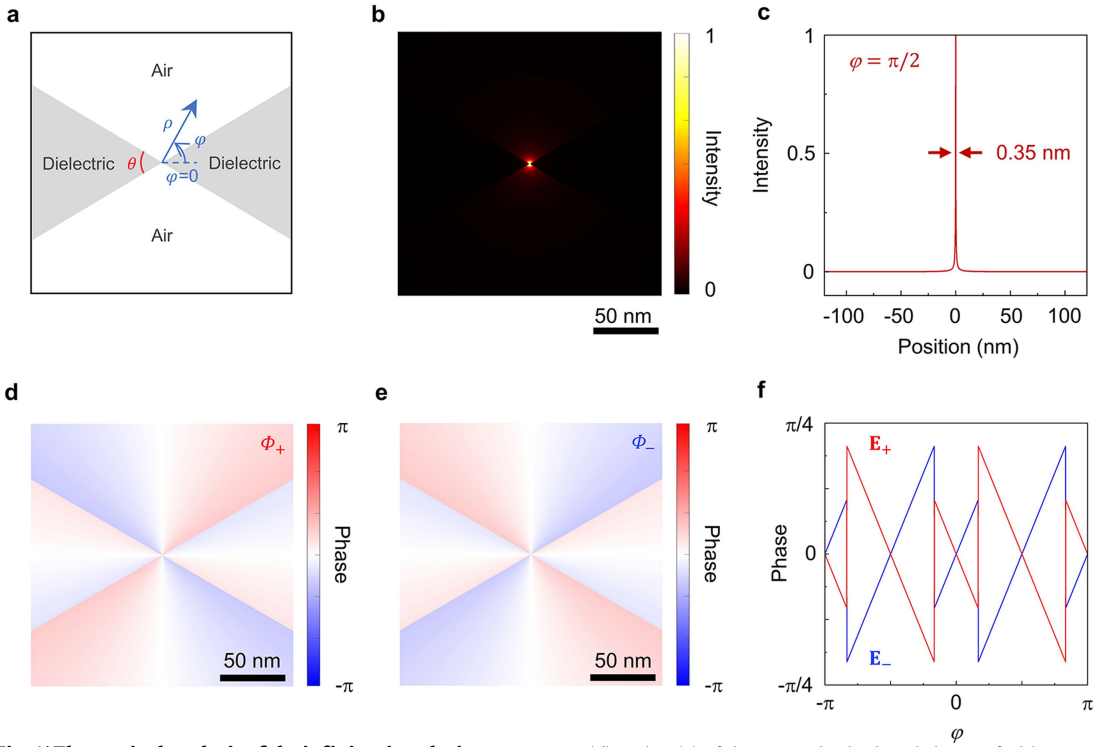

Extended Data Fig. 1 | Theoretical analysis of the infinite singularity in a singular dielectric nanolaser. a, Schematic of a dielectric bowtie nanoantenna with a negligible gap between its two apices. **b**, Theoretical calculated electric field intensity of the dielectric bowtie nanoantenna. **c**, Intensity profiles along $\varphi = \pi/2$ in (**b**), where the intensity is normalized to the position 0.1 nm away from the singularity. The field diminishes to a very small magnitude over a distance substantially shorter than the free-space wavelength due to the large k_ρ originated from infinite singularity. **d,e**, Phases Φ_+ (**d**) and Φ_- (**e**) of theoretical calculated electric field components $\mathbf{E}_\pm$ represented as $\mathbf{E}_\pm = E_\pm(\mathbf{e}_x \pm i\mathbf{e}_y)$, where $E_\pm = |E_\pm| e^{i\Phi_\pm}$. The non-integral value of the topological charge l of 0.62 stems from angular discontinuities in the dielectric constant, inducing phase jumps at the boundaries between the dielectric and air. **f**, Phase changes of $\mathbf{E}_\pm$ along a circle enclosing the apices. The integral of the phase change along the circle for both $\mathbf{E}_\pm$ yields an integer value of zero, fulfilling the periodic boundary condition.

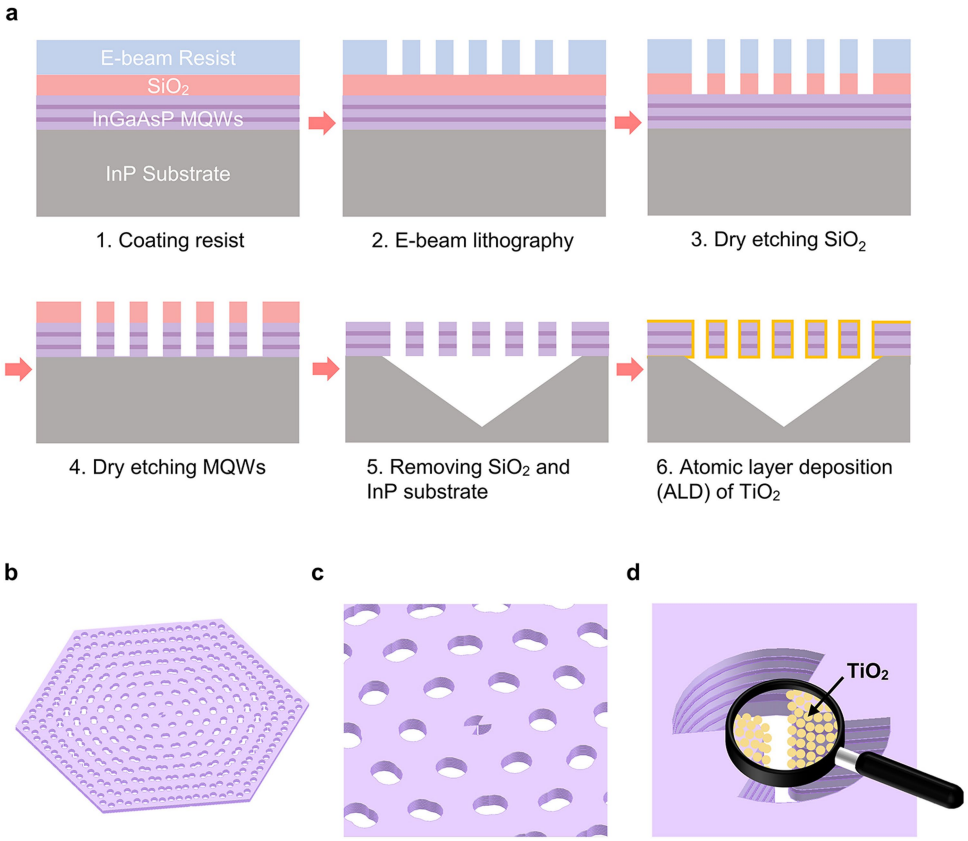

Extended Data Fig. 2 | Fabrication procedure of singular dielectric nanolasers with atomic-scale nanoantenna gap. a, Six essential steps in fabrication singular dielectric nanolaser with atomic-scale nanoantenna gap. **b-d**, Schematic diagram (**b**), and two zoomed-in version (**c,d**) of the final device.

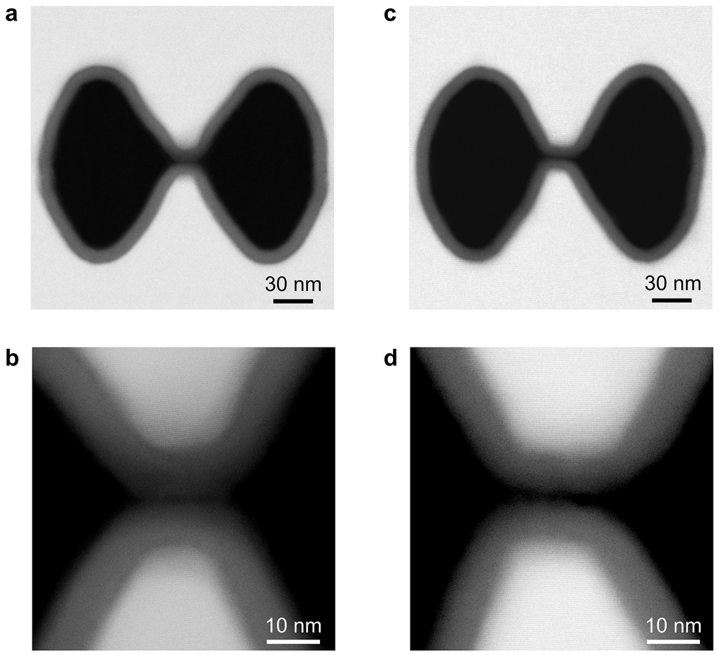

Extended Data Fig. 3 | Dark-field scanning transmission electron microscopy (STEM) images of two fabricated nanoantennas. a,b, Dark-field STEM image (**a**) and the enlarged image (**b**) of a dielectric bowtie nanoantenna with gap size that is near closure. **c,d**, Dark-field STEM image (**c**) and the enlarged image (**d**) of a dielectric bowtie nanoantenna with gap size that is close to a single nanometer. In the images, the distinction between TiO_2 and InGaAsP materials is clearly noticeable; TiO_2 appears darker in contrast to InGaAsP.

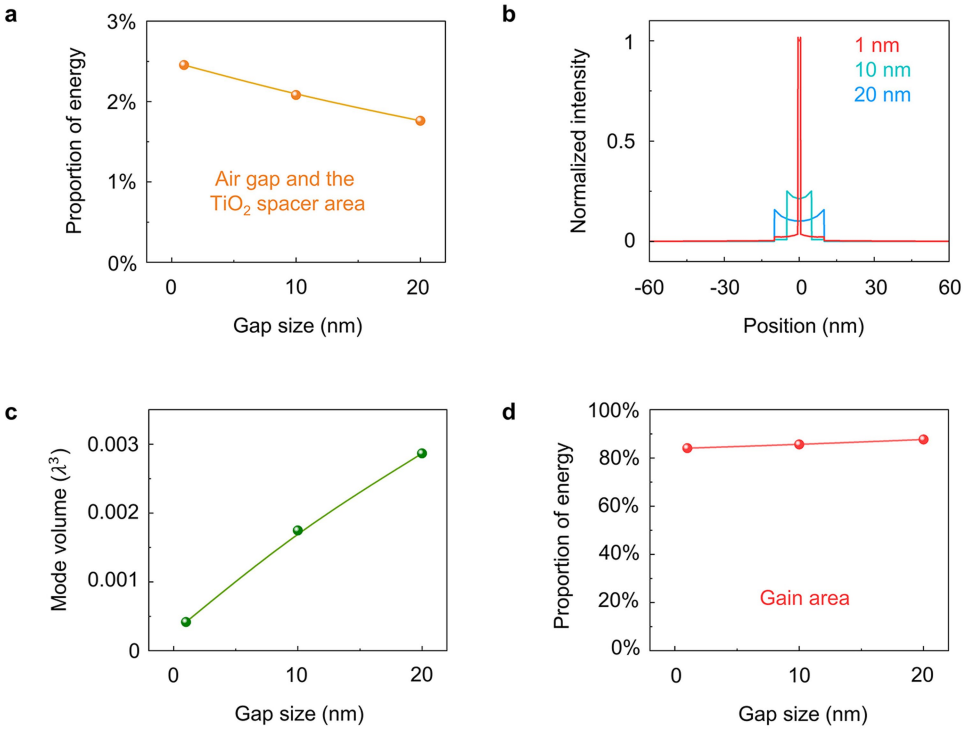

Extended Data Fig. 4 | Proportion of energy, field distribution and mode volume with varied air gap size by TiO_2 deposition. a, Proportion of energy within the air gap and TiO_2 spacer area, with a diameter of 50 nm, relative to the total mode energy for varied gap sizes. **b**, Electric field intensity at varied gap sizes, demonstrating that a decrease in gap size results in more localized electric field intensity. **c**, Mode volume at varied gap sizes. The reduction of mode volume with the decrease of the gap size is due to the redistribution of energy around the air gap area caused by the alteration in gap size as shown in (**b**). **d**, Proportion of energy within the gain area relative to the total mode energy for varied gap sizes.

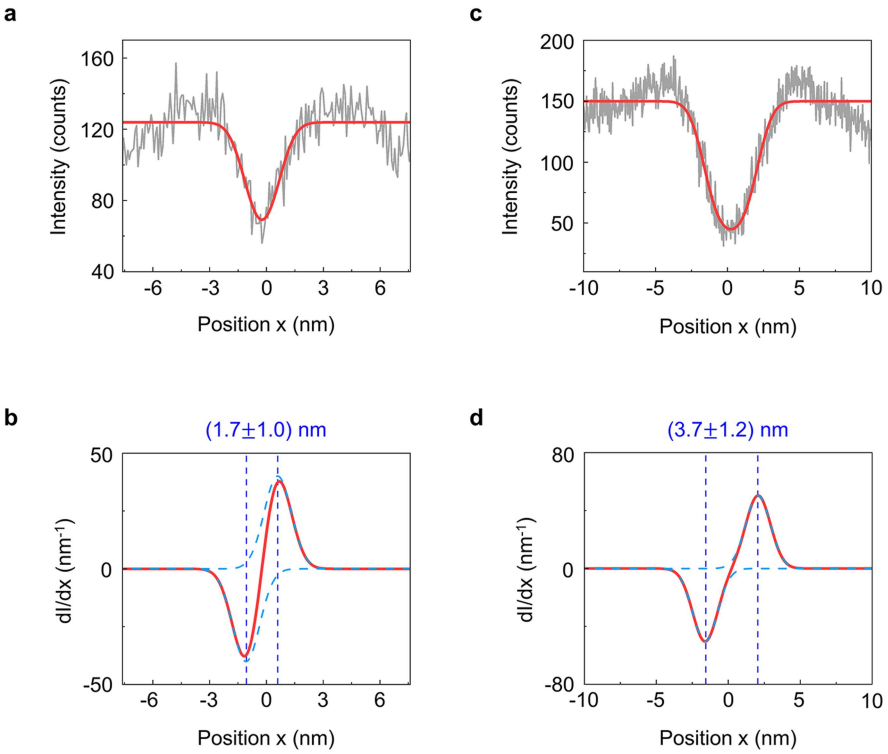

Extended Data Fig. 5 | Gap sizes determination. The two edges of the air gap are modeled using two Gaussian functions that describe the blur of the edges induced by SEM resolution, which is: $\frac{dI}{dx} = \sqrt{\frac{2}{\pi}}\frac{A}{\sigma}\left(-\exp\left(-\frac{(x-x_1)^2}{2\sigma^2}\right)+\exp\left(-\frac{(x-x_2)^2}{2\sigma^2}\right)\right)$, where x_1, x_2 denote the position of the two edges, and σ is the standard deviation of the edge positions of x_1, x_2. By integrating the first derivative of the intensity profile, we obtain the expression for the intensity profile, I, as: $I = I_0 + A\left(-\mathrm{erf}\left(\frac{x-x_1}{\sqrt{2}\sigma}\right)+\mathrm{erf}\left(\frac{x-x_2}{\sqrt{2}\sigma}\right)\right)$. This function was employed to fit the SEM image intensity profile to ascertain the values of x_1, x_2, and σ. **a**,**b**, For the device shown in Fig. 2g, the gap size, calculated as $x_2 - x_1$, with an associated standard deviation of $\sqrt{2}\sigma$, is determined to be (1.7 ± 1.0) nm. **c**,**d**, For the device shown in Fig. 2h, the gap size is determined to be (3.7 ± 1.2) nm.

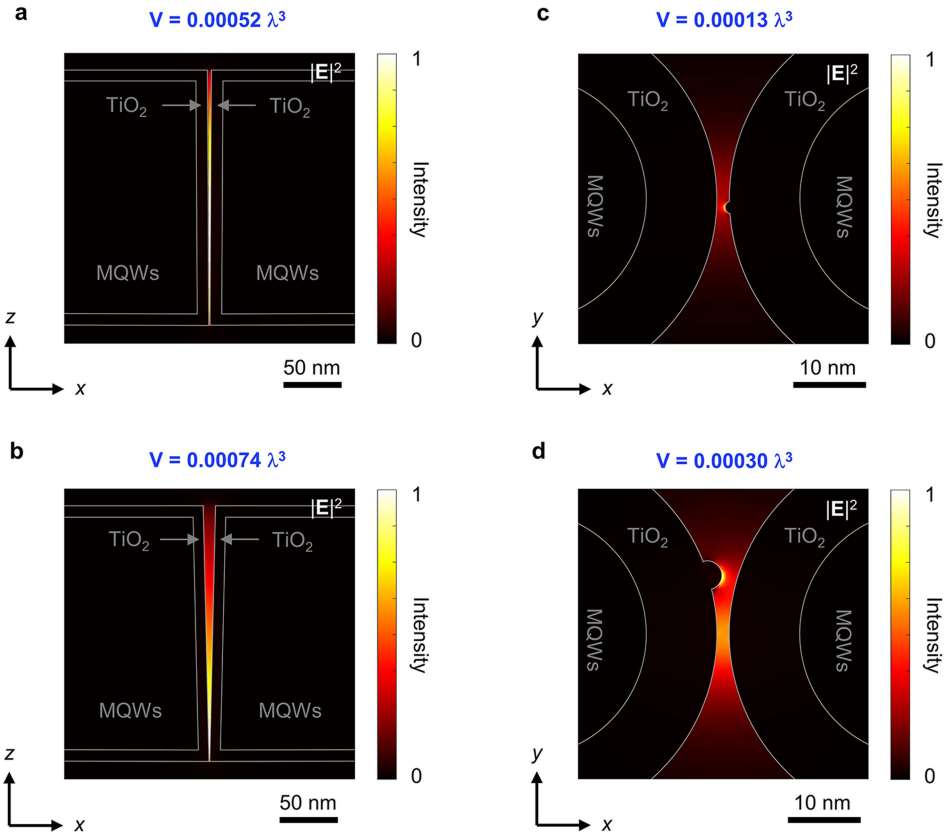

Extended Data Fig. 6 | Nanocavities with tilt angles and point defects. **a,b**, Field distributions of nanocavities with tilt angles of 0.26 degrees (**a**) and 1.3 degrees (**b**), respectively. The corresponding mode volumes are 0.00052 λ^3 and 0.00074 λ^3. **c,d**, Field distributions of nanocavities with point defects with characteristic sizes of 1 nm (**c**) and 2 nm (**d**), respectively. The corresponding mode volumes are 0.00013 λ^3 and 0.00030 λ^3.

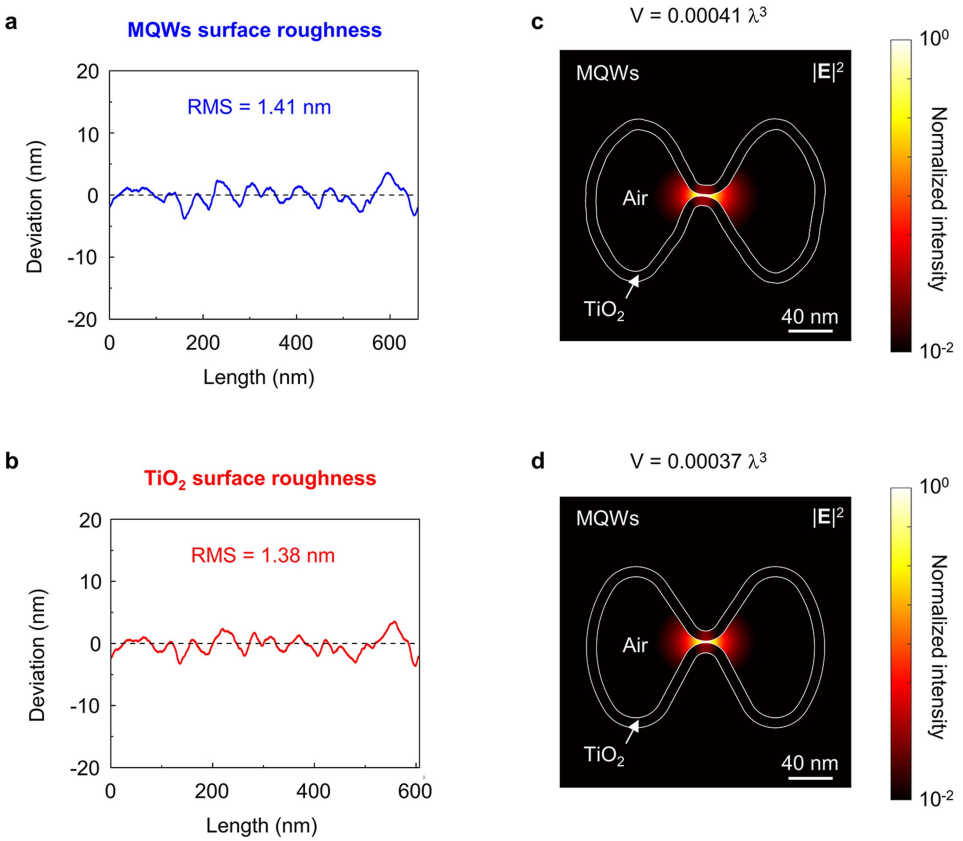

Extended Data Fig. 7 | Fabrication precision and nanocavity with surface roughness. a,b, Surface roughnesses induced by ICP etching and ALD as observed in the nanoantenna shown in Extended Data Fig. 3c,d. The root mean square (RMS) roughness from ICP etching is 1.41 nm. The surface roughness characteristic post-ALD follows the trend set by ICP etching, indicating that the ALD process forms a smooth, conformal TiO_2 layer without introducing additional roughness. **c,d**, Field distributions of nanocavities with (**c**) and without (**d**) surface roughnesses. The corresponding mode volumes are $0.00041\lambda^3$ and $0.00037\lambda^3$.

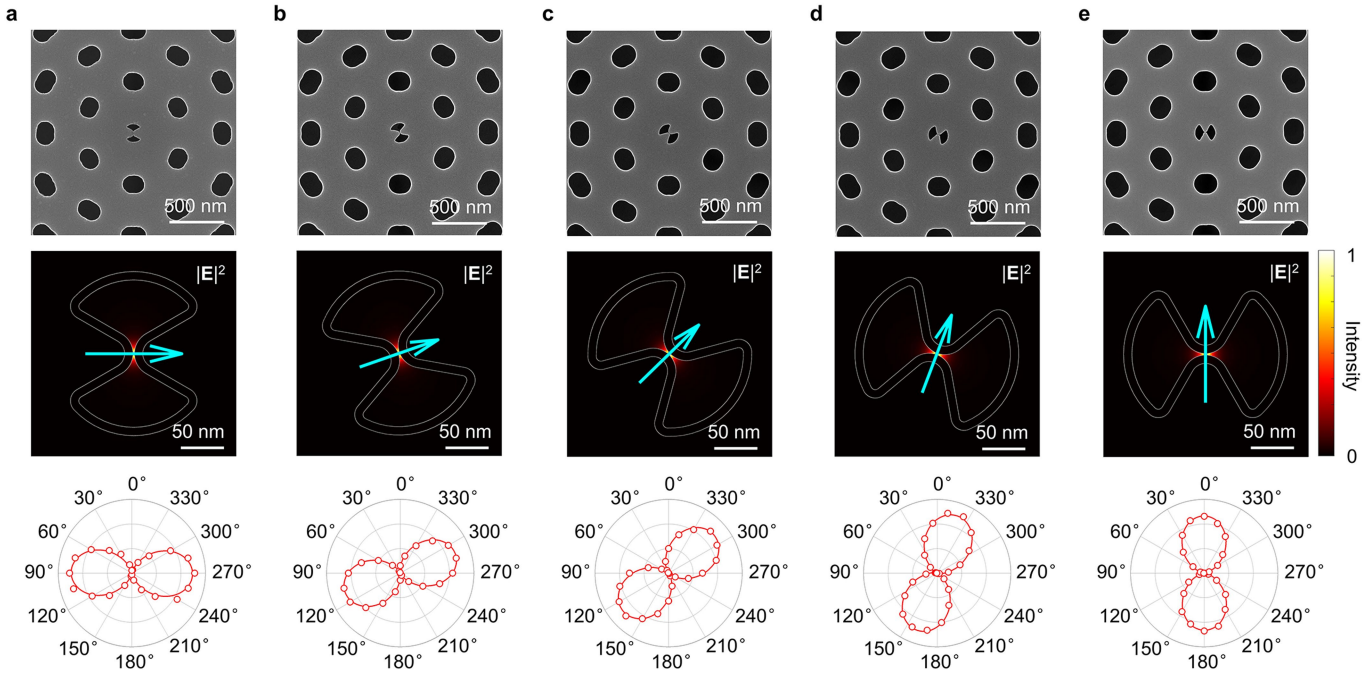

Extended Data Fig. 8 | Deterministic relationship between nanoantenna's orientation and lasing emission polarization. Panels (**a**–**e**) present a progression from left to right, showing the influence of five distinct nanoantenna orientations on the emission polarization of singular dielectric nanolasers. The top row shows SEM images, the middle row shows full-wave simulated electric field intensity distributions and polarization directions (indicated by arrows) within the cavity, and the bottom row shows experimentally measured lasing emission polarizations. Both the full-wave simulation and experimental findings demonstrate that the polarization direction of the lasing mode adjusts with the nanoantenna's rotation angle.

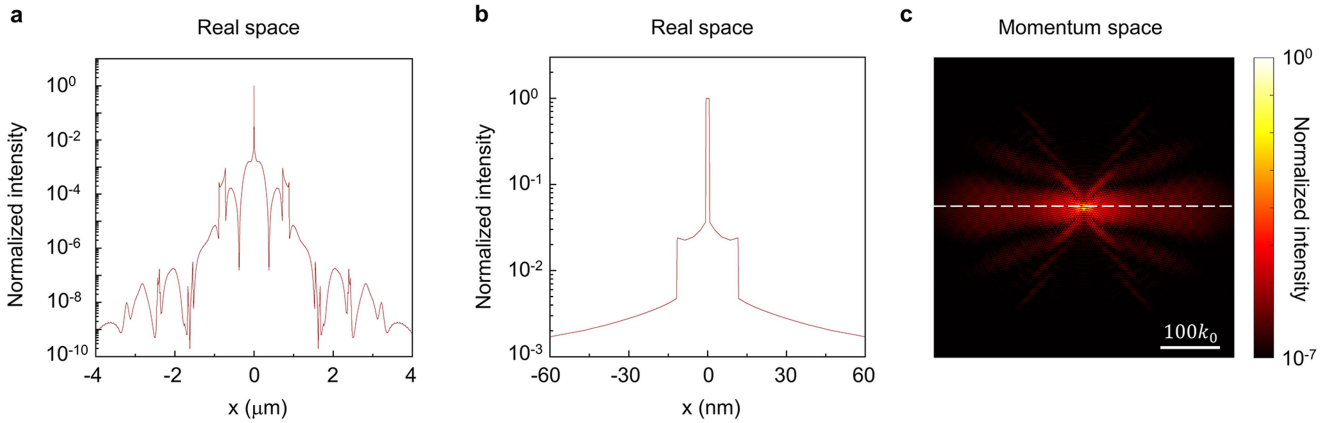

Extended Data Fig. 9 | Atomic-scale localized optical field and the corresponding large momentum distribution area of the singular dielectric nanolaser. a,b, Simulated log-scale intensity profiles depicted in Fig. 5d (**a**) and Fig. 5e (**b**), respectively. **c**, Simulated wavevector distribution of the cavity mode obtained by Fourier transforming the real-space mode pattern. k_0: free-space wavevector.

Extended Data Table 1 | Performance comparison

Type	Reference	Gain Materials	Mode volume	Wavelength	Temperature	Threshold Power density	Lasing Q factor †	Spectrum resolution (δλ) limited Q factor (λ/δλ)	Cold cavity Q factor	Purcell factor
Singular nanolaser	**This work**	**InGaAsP QWs**	**~0.0005λ^3**	**~1,580 nm**	**RT**	**~26 kW/cm^2**	**~13,200**	**~39,500**	**~5,700**	**~58**
Plasmonic nanolasers	Nature **482**, 204-207 (2012)	InGaAsP QWs	~0.002λ^3	~1,500 nm	RT	~5 MW/cm^2	~220	~2,240	264	—
	Opt. Express **21**, 4728-4733 (2013)	InGaAs	~0.67λ^3	~1,590 nm	RT	~65 kA/cm^2	~3,200	~7,950	235	13.88
	Nat. Commun. **8**, 15528 (2017)	Dye	—	~530 nm	RT	~4 MW/cm^2	~530	~5,300	—	—
	Nano Lett. **18**, 7942–7948 (2018)	CdSe	~0.05λ^3	~700 nm	RT	~13 kW/cm^2	~2,500	~7,000	—	—
	Nature **581**, 401-405 (2020)	InGaAsP QWs	~0.02λ^3 *	~1,257 nm	RT	~140 kW/cm^2	~320	~13,000	340	—
Nano-slit-waveguide laser	Phys. Rev. Lett. **129**, 013902 (2022)	CdSe	~5λ^3	~710 nm	RT	~1.4 MW/cm^2	~1,400	~20,000	~60	—
Moiré nanolasers	Nat. Nanotechnol. **16**, 1099-1105 (2021)	InGaAsP QWs	~0.01λ^3	~1,500 nm	RT	~6 kW/cm^2	~9,000	~15,000	430,000	—
	Nature **624**, 282-288 (2023)	InGaAsP QWs	~0.016λ^3	~1,605 nm	RT	~11 kW/cm^2	~6,400	~16,000	—	—
Topological lasers	Phys. Rev. Lett. **120**, 113901 (2018)	InGaAsP QWs	~0.8λ^3 *	~1,590 nm	—	—	~1,500	—	—	—
	Science **359**, eaar4005 (2018)	InGaAsP QWs	~600λ^3 *	~1,556 nm	—	~16 kW/cm^2	~4,500	~12,000	—	—
	Nat. Nanotechnol. **15**, 67-72 (2020)	InGaAsP QWs	~4λ^3 *	~1,596 nm	RT	~4 kW/cm^2	~6,400	~16,000	208	—
	Phys. Rev. Lett. **125**, 013903 (2020)	InGaAsP QWs	~2λ^3 *	~1,510 nm	RT	~120 kW/cm^2	~3,800	~15,100	—	—
	Light Sci. Appl. **9**, 109 (2020)	InGaAs QDs	~0.02λ^3	~1,170 nm	4.2 K	~0.06 kW/cm^2	~2,600	~17,700	~25,000	—
	Science **373**, 1514-1517 (2021)	InGaAs QDs	—	~953 nm	4 K	~7 kW/cm^2	~5,200	~65,000	—	—
	Science **375**, 884-888 (2022)	InGaAsP QWs	—	~1,596 nm	—	~19 kW/cm^2	~1,100	—	——	—
	Nature **608**, 692–698 (2022)	InGaAsP QWs	~70λ^3 *	~1,550 nm	RT	~29 kW/cm^2	~1,000	—	~10,000	—
	Nat. Photon. **18**, 286-392 (2023)	InGaAsP QWs	~0.02λ^3	~1,530 nm	RT	~1 kW/cm^2	~2,400	~3,060	20,000	—
BIC lasers	Nature **541**, 196-199 (2017)	InGaAsP QWs	~8λ^3 *	~1,550 nm	RT	~4 kW/cm^2	~4,700	~4,700	—	—
	Nat. Nanotechnol. **13**, 1042-1047 (2018)	GaAs	~500λ^3 *	~825 nm	77 K	~70 MW/cm^2	~2,750	~8,000	—	—
	Nat. Commun. **12**, 4135 (2021)	InGaAsP QWs	~36λ^3 *	~1,595 nm	RT	~1 kW/cm^2	~7,300	~7,300	—	—
	Laser Photon. Rev. **15**, 2000411 (2021)	Dye	—	~614 nm	RT	~100 kW/cm^2	~614	—	—	—
	Nat. Photon. **15**, 758-764 (2021)	InGaAsP QW	~0.07λ^3	~1,560 nm	RT	~10 kW/cm^2	~78,000	~78,000	—	—
	Nat. Commun. **13**, 6485 (2022)	InGaAsP QWs	~48λ^3 *	~1,567 nm	RT	~1 kW/cm^2	~11,000	~15,700	—	—
	Science **377**, 1215-1218 (2022)	Dye	~700 λ^3 *	~610 nm	RT	~22 mJ/cm^2	~1,250	—	—	—
Photonic crystal defect-cavity lasers	Nat. Photon. **9**, 311-315 (2015)	InGaAs/InGaAsP QWs	~0.02λ^3	~1,540 nm	RT	~71 kW/cm^2	~5,000	~15,400	~100,000	~2
	Nat. Commun. **6**, 8276 (2015)	InGaAsP QW	~0.02λ^3 *	~1,520 nm	RT	~0.02 kW/cm^2	~3,800	~3,800	92,000	—
	ACS Photonics **4**, 2117-2123 (2017)	InGaAsP QWs	~0.007λ^3	~1,556 nm	RT	~2 kW/cm^2	~400	—	1,100	—
	Nano Lett. **17**, 1892-1898 (2017)	InGaAsP QWs	~0.06λ^3 *	~1,491 nm	RT	~7 kW/cm^2	~2,100	—	2,580	—
	Nat. Photon. **11**, 81-84 (2017)	InAs QDs	~0.06λ^3	~1,566 nm	RT	~65 kW/cm^2	~2,600	—	800	—
	Opt. Express **29**, 26082-26092 (2021)	InGaAsP QWs	~0.03λ^3 *	~1,558 nm	RT	~2 kA/cm^2	~66,000	—	1,500	—

BIC: bound states in the continuum; QW: quantum well; QD: quantum dot; RT: room temperature; Q factor: quality factor;

*: Mode volume is estimated from the physical volume of the device;

†: Lasing quality factor is calculated as lasing wavelength over linewidth (λ/Δλ).